RSC Applied Interfaces

ROYAL SOCIETY OF CHEMISTRY

PAPER

View Article Online
View Journal | View Issue

Cite this: *RSC Appl. Interfaces*, 2025, **2**, 1913

Exploring the influence of anodization-derived nanotubular and honeycomb surfaces on the osteogenic behaviour of human MG63 osteoblastic cells

Ryan Berthelot [ab] and Fabio Variola *[abcd]

Nanoscale topography plays a pivotal role in modulating cellular behavior and has been a key parameter in the design of cell-instructive surfaces for biomedical applications. This study investigates the differential effects of two anodized titanium surfaces – a conventional nanotubular (NT) surface (~75 nm diameter) and a two-tier honeycomb (HC) architecture – on the response of human MG63 osteoblastic cells. The HC surface, characterized by higher spatial entropy and a complex arrangement of smaller nanotubes (~7 nm in diameter) clustered within larger domains (~109 nm in diameter), significantly enhances early cellular functions, including proliferation, viability and upregulation of osteogenic markers (RUNX2, OSX, ALP), with the YAP/Hippo pathway likely implicated as a key mediator. This is evidenced by increased focal adhesions and nuclear YAP1 localization, underscoring the HC surface's capacity to promote cellular attachment and early differentiation. Conversely, the NT surface, with its more ordered nanotube array, induces comparable mineralization but yields higher-quality mineral deposits enriched with crystalline hydroxyapatite, suggesting greater efficacy in supporting mature mineral formation. These findings highlight the selective influence of nanotopographical features on early cellular dynamics *versus* long-term mineralization, offering critical insights into structure–function relationships governing MG63 cellular response to anodized titanium. By demonstrating the HC surface's prowess in early osteogenesis and the NT surface's strength in stable mineral deposition, this research advances the design of cell-instructive biomaterials tailored to distinct phases of bone regeneration, with implications for tissue engineering and biomedical implant technology.

Received 4th July 2025,
Accepted 13th October 2025

DOI: 10.1039/d5lf00190k

rsc.li/RSCApplInter

Introduction

The surface properties of biomaterials dictate their interactions with the surrounding biological environment by influencing cellular behavior and, ultimately, the tissue integration and performance of biomedical implants.[1–4] In particular, the role of the nanoscale topography has attracted significant attention for its ability to modulate key cellular processes such as adhesion, proliferation and differentiation, among others.[5–20] The resulting interest in effective cell-instructive surfaces has, in turn, also driven the development of experimental methods and strategies to fabricate tailor-made nanoscale topographies capable of predictably eliciting specific cellular functions.[21–23] Among these, anodization has emerged as a versatile and scalable technique to endow titanium with an enhanced bioactivity resulting from the formation of an anodic TiO_2 surface layer consisting of vertically aligned hollow nanotubes with diameters ranging from tens to hundreds of nanometers.[14–17,24] One of the main advantages of anodization is its ability to precisely tune the nanotubes' diameter, a feature that has been extensively leveraged to elucidate cellular response to variable nanoscale topographies.[10,25–29] In this context, our group has explored the biological potential of a two-tier honeycomb (HC) architecture resulting from the controlled anodization of titanium, demonstrating that this surface, consisting of smaller nanotubes (HC-T1) clustered within larger domains (HC-T2), significantly enhances various cellular functions (*e.g.* viability, migration, mineral deposition) when compared to conventional single-tier nanotubular structures.[30,31] However, although we have postulated a key role of the higher spatial entropy associated with the HC architecture to explain these findings,[5,10,12,25,28,32–37] the underlying mechanisms

[a] *Faculty of Engineering, Department of Mechanical Engineering, University of Ottawa, Canada. E-mail: Fabio.variola@uottawa.ca*
[b] *Ottawa-Carleton Institute for Biomedical Engineering (OCIBME), Ottawa, Canada*
[c] *Department of Cellular and Molecular Medicine, University of Ottawa, Canada*
[d] *Children's Hospital of Eastern Ontario (CHEO), Ottawa, Canada*

responsible for the observed cellular differences still remain to be elucidated.

To bridge this gap, the present study aims to conduct a comparative analysis of the two-tier honeycomb architecture and a conventional nanotubular (NT) surface (~75 nm in diameter) with respect to their ability to influence the response of human MG63 osteoblastic cells. The choice of this particular NT surface was motivated by its relatively low spatial entropy deriving from a highly ordered nanotube arrays and by the fact that previous work indicated this dimension as the optimal diameter to elicit osteogenic functions, thereby making it a suitable reference for comparison.[38–41] Notably, the HC-T2 tier shares similarities with the NT surface in terms of structural entropy and the N1 : N6 ratio (Fig. 1), and its shallow depth (~30 nm) is believed to only have limited impact on cellular functions such as integrin clustering.[30,31] This ultimately minimizes the influence of these shared structural variables in our analysis. Consequently, observed differences in cellular response can be primarily attributed to the unique features of the HC-T1 tier, such as its distinct topography and dimensions, rather than to those of the HC-T2 tier.

Collectively, results from this study show that the HC surface, with its more disordered spatial metrics (lacunarity, fractal dimension and entropy) promotes early cell proliferation and differentiation, evidenced by increased viability, mitochondrial activity and upregulation of osteogenic markers (RUNX2, OSX and ALP). Notably, the YAP/Hippo pathway was identified as a potential key mediator for

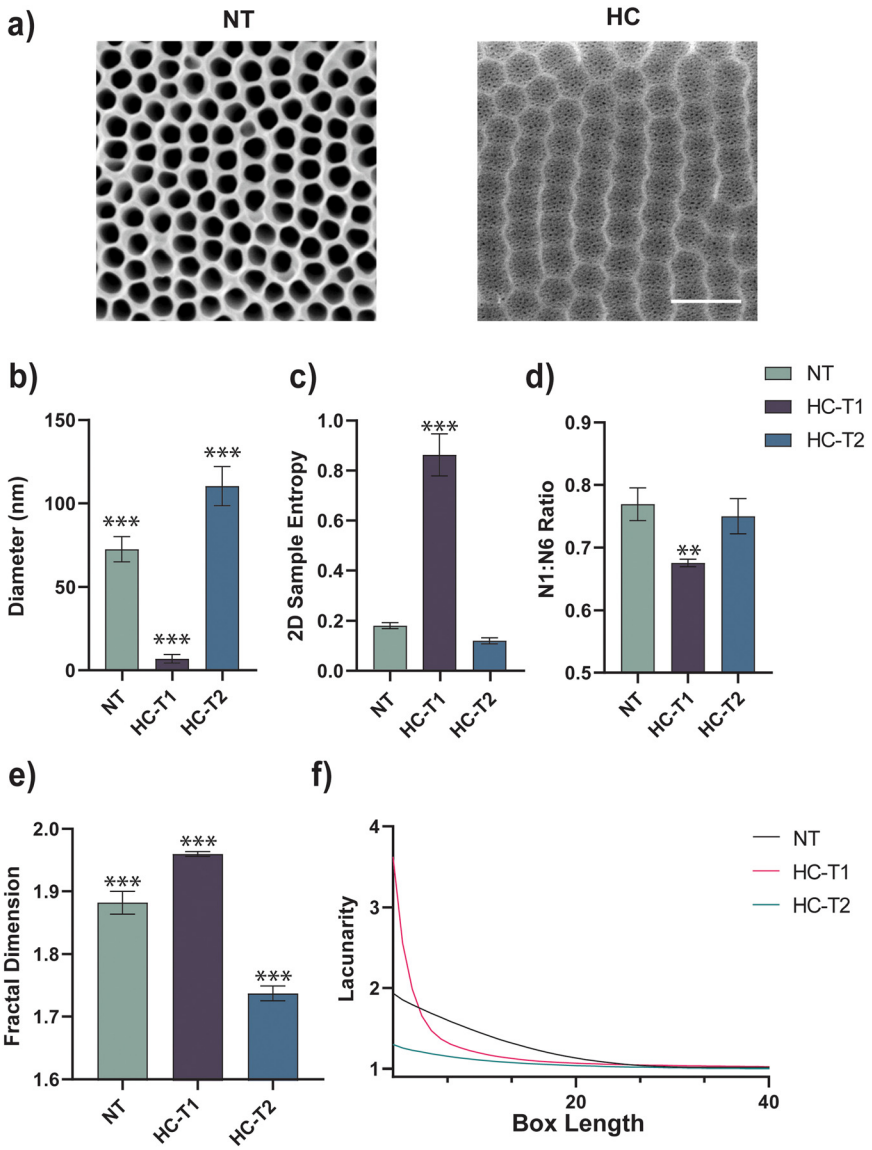

Fig. 1 SEM images and spatial metrics of the NT and HC surfaces. a) SEM micrographs of the NT surface (left) and the HC architecture (right). Scale bar: 200 nm. b) Nanotube diameter for the NT and the HC surfaces. Spatial statistics: c) surface entropy, d) N1 : N6 ratio, e) fractal dimension and f) lacunarity.

these early osteogenic functions. In contrast, the NT surface elicits more marked later-term events, inducing the formation of mineral deposits with a higher degree of crystallinity. Taken together, these findings further underscore the selective role of specific nanoscale topographies in shaping both early cellular response and long-term mineralization, while providing new insights into the differential cueing exerted by the NT and HC nanostructures. In conclusion, this work not only deepens our understanding of how nanotopography influences cellular behavior but also suggests a framework for tailoring cell-instructive surfaces for titanium biomedical implants to optimize distinct phases of bone regeneration.

Experimental

Anodization of titanium

Titanium foil (0.127 mm thickness, 99.9+% purity, Thermo Fisher, USA) was cut into 2.5 × 1 cm strips. These were subsequently immersed in 99.8% anhydrous toluene (Sigma-Aldrich, USA) and subjected to sonication for 15 minutes to remove surface contaminants. After sonication, the strips were thoroughly rinsed with deionized water and allowed to air-dry. Samples were mounted in a 3D-printed fixture made of UV-hardened resin, where they were aligned parallel to a 2.5 cm × 2.5 cm platinum electrode (99.9% purity, Alfa Aesar, USA) *via* alligator clips, ensuring stability throughout the process. The anodization process was carried out with a Bio-Rad PowerPac power supply (Bio-Rad, USA) under constant DC voltage in a 50 ml Pyrex beaker filled with anhydrous ethylene glycol ($C_2H_6O_2$, Sigma-Aldrich) mixed with 0.3 wt% crystalline ammonium fluoride (NH_4F, Sigma-Aldrich) and 2 wt% deionized water. Voltages below 20 V were applied using a B&K Precision model 9111 power supply (B&K Precision Corporation, USA). The resulting anodic oxide layer was removed with adhesive tape, and the samples were re-mounted for a second anodization step. Upon completion, surfaces were rinsed with deionized water and air-dried. By adjusting the parameters of each anodization step (Table 1), the two nanostructures considered in this study were generated.

SEM characterization and analysis of anodized surfaces

The nanoscale surface morphology of the anodized substrates was imaged by using a Gemini 500 Scanning Electron Microscope (Zeiss, Germany) at a magnification of 50 000×. SEM images were processed with a custom ImageJ[42] pipeline, where they were manually thresholded, segmented, and analyzed using the 'Particle Analysis' tool. Nanotube diameters were calculated using this tool, with outliers removed by applying a 0.1% *Q* value. Entropy was quantified to assess the randomness and complexity of pixel intensity values within the images. The analysis was performed using the SampEn2D plugin in ImageJ, with $m = 2$ and r set as a fraction (0.2) of the standard deviation of pixel values.[43,44] This analysis evaluates the probability that sequences of data points that are similar for m points remain similar at the next point within a tolerance r.[45,46] The hexagonal packing efficiency of the nanotubes was assessed using the N1 : N6 ratio, defined as the ratio of the first nearest neighbor distance (NND) to the average of the six nearest neighbor distances.[47] This metric quantitatively measures how closely the nanotube arrangements approximate the ideal hexagonal packing. Fractal dimension was calculated to quantify the complexity of the nanotubular patterns. The box-counting method was employed, where a grid of boxes of varying sizes is superimposed onto the image, and the number of boxes containing part of the structure is counted. The fractal dimension was derived from the slope of the log–log plot of the number of boxes *versus* the box size, and was carried out by using the MultiFrac[48] plugin in ImageJ.[49] Lacunarity was calculated to measure the texture and spatial distribution of gaps within the nanotubular structures. This was accomplished by using the gliding box method, which involves covering the image with a series of boxes of varying sizes and calculating the variance in the number of occupied boxes across scales. The analysis was performed using the MultiFrac[48] plugin in ImageJ, covering a range of box sizes to capture the multi-scale heterogeneity. To ensure consistency in the analysis, images were processed in ImageJ and converted into binary format, with nanotubes represented as white pixels on a black background. Outlier removal was conducted using the ROUT method with a *Q* value of 0.1% to maintain data integrity while eliminating extreme values.

Table 1 Voltage and time parameters for the NT and HC surfaces

		NT	HC
Step 1	Voltage (V)	60	60
	Time (min)	30	30
Step 2	Voltage (V)	60	5
	Time (min)	10	5

Human MG63 osteoblastic cell cultures

Human MG63 osteoblastic cells (CRL-1427, ATCC, USA) were thawed and passaged in DMEM (10567-014, Gibco, USA) containing 5 mM glucose, supplemented with 10% fetal bovine serum (FBS), 10 mM β-glycerophosphate and 50 μg mL^{-1} ascorbic acid. The cells were maintained at 37 °C in a humidified atmosphere of 5% CO_2. After gently aspirating the complete culture medium (CCM), cells were gently washed three times with sterile 1× PBS. To detach the cells, 3 mL of 1× TrypLE were added to the flask for a 3-minute incubation to ensure complete detachment. The cell suspension was diluted by adding 7 mL of culture medium and subsequently centrifuged at 150 rpm for 8 minutes. After centrifugation, the cells were resuspended in 10 mL of CCM. A 2 mL aliquot of the cell suspension was transferred into 8 mL of fresh CCM in a filtered 75 cm^2 flask, which was returned to the incubator for continued culture.

Cell seeding and fixation

NT and HC substrates were sterilized in 70% ethanol and subsequently rinsed with sterile 1× phosphate-buffered saline (PBS). Cells for all immunofluorescence and Raman analyses were seeded onto the substrates at a density of 5000 cells per cm^2 in 60 mm tissue-culture treated Petri dishes. Surfaces were removed and placed in 24-well plates and the cells were cultured on the nanotubular substrates for durations specific to each experiment, ranging from 1 to 21 days, to investigate proliferation, morphology, establishment of focal adhesions/complexes, differentiation and mineral deposition. At the conclusion of the experiments, cells were fixed by adding 500 μL of fresh 4% paraformaldehyde (PFA, Sigma-Aldrich) to each well for 10 minutes at room temperature (RT). The wells were then washed three times with PBS to remove any residual PFA, filled with 500 μL of PBS, and stored at 4 °C. Day 21 mineral samples underwent a separate fixation with methanol. After aspirating the culture medium, cells were rinsed once with PBS and then with distilled water. The samples were then immersed in pre-cooled methanol (−20 °C) for 10 minutes at RT. Following fixation, the methanol was removed, and the samples were allowed to air-dry completely. The dried, fixed samples were stored at RT until analysis.

Immunofluorescence staining

MG63 cells were permeabilized with a 0.25% solution of Triton X-100 (TX-100, Sigma-Aldrich) for a duration of 10 minutes at RT. Following permeabilization, samples were blocked with 5% Donkey serum (Sigma-Aldrich) at RT for 1 hour. Nuclei and actin filaments were labeled with DAPI and 1 : 400 AlexaFluor 488 Phalloidin (Thermo Fisher). Vinculin, active YAP1 and osterix (OSX) were stained with primary anti-hVin1 mouse mAb (Sigma-Aldrich) at a ratio of 1 : 500, YAP1 monoclonal antibody (Proteintech, USA) at a ratio of 1 : 400 and anti-OSX mAb (SP7 monoclonal antibody (2G6)) (Thermo Fisher) at a 1 : 100 dilution, respectively. These primary antibodies were followed by secondary staining using AlexaFluor 594 Donkey-anti-mouse IgG (Thermo Fisher) at a 1 : 500 dilution. Cell proliferation was assessed by staining for anti-Ki-67 polyclonal rabbit antibody (Millipore Sigma, USA) at a 1 : 250 dilution, while RUNX2 polyclonal rAb (Thermo Fisher) at a 1 : 100 dilution was used as a second differentiation marker. YAP1 was stained using phospho-YAP1 (ser127) (Thermo Fisher) at a dilution of 1 : 100. RUNX2, phospho-YAP1 and Ki-67 primary stains were followed by secondary labeling with AlexaFluor 647 Donkey-anti-rabbit IgG (Thermo Fisher). The primary antibody incubation was conducted overnight at a temperature of 4 °C, whereas the blocking and secondary antibody incubations were each carried out for 1 hour at RT. Post-incubation, the samples were thoroughly washed and subsequently imaged in PBS in a 60 mm Petri dish.

Immunofluorescence imaging and analysis

The multi-channel images used for the quantification of nuclei number and the analysis of cytoskeletal morphology were obtained by using a ThermoFisher EVOS FL Auto 2 (inverted) widefield microscope (ThermoFisher, USA). Images for all immunofluorescence experiments were captured with a 20× air objective (20×, 0.40 NA, air, PL FL LWD PH). The imaging system utilizes LED light sources with specific filters for different wavelengths: blue (Ex 357/44 nm, Em 447/60 nm), green (Ex 470/22 nm, Em 510/42 nm), red (Ex 585/29 nm, Em 624/40 nm), and far red (Ex 628/40 nm, Em 692/40 nm). Detection is performed using a monochrome camera. For day 1 samples, 3 images were analyzed as technical replicates, each consisting of 9 images stitched together (total 27 images). For day 3 and day 5 samples, 6 images per sample were taken at randomly selected locations across each sample. The number of DAPI-stained nuclei and actin morphology were quantified with custom ImageJ[42] pipelines. Both nuclear and cellular morphology analyses were carried out by stitching, segmenting and processing images in a custom pipeline calculated *via* particle analysis in ImageJ.

DAPI images were segmented *via* custom ImageJ pipeline and used in generating regions of interest (ROIs) for measuring nuclear intensities and total expression for Ki-67, active YAP1, OSX and RUNX2. Actin images were also segmented in ImageJ and used in generating regions of interest (ROIs) for measuring nuclear intensities and total expression YAP1 and cytoplasmic OSX. Total protein expression as defined as the integrated density of the ROI. For Ki-67 analysis a minimum of 15 samples per condition were analyzed, encompassing three biological replicates from each of nine distinct experimental sets, discarding one sample to use as a negative control. The active YAP1/YAP1 ratio was calculated by dividing the mean intensities of active YAP1 ROIs by the mean intensities of the YAP1 ROIs. In a similar way, the OSX NucBod Ratio was calculated by dividing the mean intensity of nuclear bound OSX by the mean intensity of OSX present in the cytoplasm. Vinculin images were subject to a background subtraction and auto-thresholding *via* a custom ImageJ pipeline and resulting segmented images were analyzed *via* the "Particle Analysis" tool in ImageJ. Focal complexes were defined as having a length along the major axis being less than 2 μm and focal adhesions having a major axis length greater than 2 μm, but less than 10 μm.[50–52] All day 1 immunofluorescence experiments consisted of 14 samples per condition, analyzed across three separate experiments, with 1 damaged sample being discarded. Day 3 and day 5 immunofluorescence experiments consisted of 20 samples per condition, across three separate experiments.

Proliferation assay

The PrestoBlue assay (Thermo Fisher) was employed to assess cell viability in response to their metabolic activity. Cells were first seeded in a 48-well plate at a density of 5000 cells per

cm^2 and cultured at 37 °C. PrestoBlue measurements were taken at 1-, 3- and 5-day intervals. The PrestoBlue reagent was diluted 1 : 10 in CCM as a working solution. The culture medium was removed from the wells and 250 μL of the prepared PrestoBlue working solution were added to each well. The plate was incubated at 37 °C with 5% CO_2 for 1 hour. Following the incubation period, the plate was gently swirled to ensure even distribution of the reagent and cells. Two 100 μL aliquots of solution were transferred to a 96-well plate as technical replicates, while fresh CCM was pipetted back into the 48-well plate. Fluorescence signal was measured with the Synergy H1 plate reader (BioTek, USA) with excitation and emission wavelengths set at 560 nm and 590 nm, respectively. Data analysis was carried out by subtracting intensity readings of control wells containing only media and the 1 : 10 PrestoBlue mixture and comparing the relative fluorescence units between anodized and control groups to determine the effect of various treatments on cell viability/metabolism. This assay was completed in triplicate with 10 wells per condition, per plate per experiment (30 samples in total).

Alkaline phosphatase (ALP) assay protocol

The alkaline phosphatase (ALP) activity was evaluated at two different time points, namely 3- and 5-day post seeding, by employing the Pierce PNPP Substrate kit (Thermo Scientific, USA). Cells were first seeded in a 48-well plate at a density of 5000 cells per cm^2 and cultured at 37 °C. Following each predetermined incubation period, samples were subjected to lysis and then treated with a solution made from *p*-nitrophenyl phosphate, disodium salt (PNPP) tablets and 1 M diethanolamine, as per the guidelines provided by the manufacturer. The reaction was allowed to proceed for 1 hour before it was terminated by adding NaOH. Subsequently, ALP activity was quantified by measuring the absorbance at 405 nm using the Synergy H1 plate reader (BioTek, USA). To maintain consistency across multiple time points, all ALP measurements were juxtaposed with a standard curve. All experiments were done in triplicate with a total of 30 samples, with 10 wells for each experimental condition across 3 independent experiments.

Alizarin red staining assay

To assess mineralization, an alizarin red staining (ARS) (Sigma-Aldrich) protocol was employed. Cells were first seeded on 0.5 × 0.5 cm NT and HC samples placed in a 48-well plate at a density of 5000 cells per cm^2 and cultured at 37 °C and grown for 21 days. Initially, the culture medium was carefully discarded from each well, followed by a gentle triple washing step in 1× PBS. Cells were fixed in 4% PFA at RT for approximately 15 min. Following the fixation, the PFA was removed, and the cells were subjected to three thorough washing steps in deionized water. After ensuring the complete removal of deionized water, each well was treated with 1 mL of 40 mM ARS solution. This step involved a RT incubation period of 25 min, during which the plates were subjected to gentle shaking to ensure optimal interaction between the cells and the dye. Post-incubation, the ARS solution was removed, and the cells were washed 5 times with deionized water to eliminate the reagent. As a final step, the plates were tilted for about 2 minutes to facilitate the removal of any residual water, thereby preparing the samples for subsequent procedures and analyses.

After imaging, 200 μL of 10% acetic acid were first added to each well and incubation was completed at RT for 30 minutes with shaking. Cells were successively collected using a cell scraper and transferred to a 1.5 mL microcentrifuge tube containing the 10% acetic acid. The samples were then subjected to vortexing for 30 seconds and heated at 85 °C for 10 minutes. To avoid evaporation, the tubes were sealed with parafilm. After the heating step, the tubes were placed on ice for a 5 min incubation period until fully cooled. Subsequently, the mixture was centrifuged at 12 000*g* for 15 minutes. Post centrifugation, the supernatant was carefully transferred to a new tube. To this, 30 μL of 10% ammonium hydroxide was added to maintain a pH between 4.1 and 4.5. 100 μL of the samples were aliquoted into a 96-well plate and the absorbance was read at 405 nm using the Synergy H1 plate reader (BioTek). Measurements for the assay were conducted on a total of 30 samples, which included nine wells from each of the three distinct experimental sets.

Confocal Raman spectroscopy

All Raman spectra were acquired using an Alpha 300R confocal Raman Microscope (WITec, Germany). The imaging system was equipped with a 50 μm diameter optical fiber (pinhole). For spectral acquisition, a Zeiss 50× EC Epiplan air objective was used. Prior to data collection, the Raman microscope system was calibrated using the silicon peak at 520 cm^{-1}. A 633 nm laser with a 1200 mm^{-1} grating and the 50× objective were used, operating at 32.7 mW.

For the analysis of mineralized deposits at day 21, cells fixed on the NT and HC surfaces were rehydrated in deionized water, scraped and dried onto CaF_2 substrates. Data analysis was conducted with the Origin Pro software (OriginLab, USA), and involved the use of the quick peaks automated peak analyzer, which provided measurements for peak position, maximum intensity, full width at half maximum (FWHM), and integrated area. A straight-line baseline was applied during the peak analysis to ensure consistency across measurements. Raman imaging and data analysis were conducted using WITec Project 4.1 Pro software. To ensure high-quality data, all images underwent spectral subtraction to remove the contributions from PBS and other background contributions. This was followed by Savitzky–Golay smoothing (parameters: 3, 3, 2, 0), cosmic ray removal (CRR) (parameters: 4, 4) and a background shape subtraction (parameters: 50, 2). Spectral averages of the samples were generated using the spectral average tool

within Project 4.1 Pro, which provided a representative spectrum for each Raman map after applying the same preprocessing steps (Savitzky–Golay smoothing, cosmic ray removal and background subtraction).

The principal Raman bands used for quantitative analysis include the amorphous calcium phosphate at ~940 cm^{-1} and the phosphate (PO_4^{3-}) ν_1 band at ~960 cm^{-1}, the carbonate (CO_3^{2-}) ν_1 band at ~1070 cm^{-1} and the amide I at ~1660–1680 cm^{-1}.[30] To assess the mineral quality, the $\nu_1(PO_4^{3-})$/amide I (mineral-to-matrix ratio, a measure of the mineral content), amorphous/$\nu_1(PO_4^{3-})$ (amorphous-to-crystalline ratio) and $\nu_1(CO_3^{2-})/\nu_1(PO_4^{3-})$ (carbonate content of the mineral) ratios were calculated. Mineral crystallinity was calculated from the 1/FWHM of the phosphate ν_1 band.

Statistical analysis

The Shapiro–Wilk test was used to evaluate the normal distribution of the datasets. For comparisons involving 2-sample conditions, if the data followed a normal distribution, a parametric Student's *t*-test was used to compare means between the two groups. For datasets that did not meet the normality assumption, the non-parametric Mann–Whitney *U* test was applied. Levene's test was conducted to evaluate the equality of variances between groups. In cases where variances were unequal, Welch's *t*-test was utilized as an alternative to the Student's *t*-test. Comparisons across timepoints involving more than two variables were analyzed using a parametric one-way ANOVA, and any significant differences in means were identified using Tukey's honest significant difference (HSD) *post hoc* test. Data deviating from normal were confirmed by the nonparametric Kruskal–Wallis test, and subject to Dunn's *post hoc* test. Error bars are displayed as the mean with 95% confidence interval, unless stated otherwise in figure description. A *p*-value less than 0.05 was considered indicative of statistical significance. The levels of significance were denoted as follows: "*" for $p < 0.05$, "**" for $p < 0.01$, and "***" for $p < 0.001$.

Results and discussion

SEM images (Fig. 1a) display the nanoscale morphology of the single nanotube structure and the unique two-tiered architecture. The NT surface exhibits the characteristic ordered array of anodized titanium, in this case consisting of nanotubes of 72 ± 8 nm in diameter (Fig. 1b). Conversely, the HC architecture features two superimposed tiers with significantly different diameters: 7 ± 2.5 nm (HC-T1) and 109 ± 12 nm (HC-T2). Surface entropy (Fig. 1c) highlights the disordered nature of the HC-T1 domains, which exhibit significantly higher values compared to the other architectures. In this context, the fact that HC-T2 domains, despite their larger diameter, do not show a significant difference in entropy from the NT surface suggests that the spatial arrangement of nanotubes, rather than size alone, plays a crucial role in determining the surface's overall complexity. The analysis of hexagonal packing efficiency, as measured by the N1 : N6 ratio (Fig. 1d), further underscores the differences between these surfaces. The HC-T1 nanotubes, with their less efficient packing and higher disorder, contrast with the more organized packing found in the HC-T2 and NT domains. These differences in entropy and packing efficiency are crucial as findings in previous literature emphasize the importance of entropy and disorder in influencing cellular interactions and response, guiding cells more effectively into differentiation.[17,53–55] The significantly different fractal dimension values across all surfaces (Fig. 1e), with the HC-T1 surface exhibiting the highest value and the HC-T2 surface the lowest, illustrate the hierarchical nature of the HC architecture. In fact, a higher fractal dimension often indicates a more complex surface[49] capable of presenting multiple scales of topographical features to adhering cells, which could enhance cellular functions such as differentiation and proliferation, complementing the N1 : N6 packing metric. In contrast, the lower fractal dimension of the HC-T2 domains suggests a simpler, more homogeneous structure. Lacunarity, which measures the texture and spatial distribution of gaps within the nanotubular arrays, also varies significantly between the surfaces (Fig. 1f).[56] The highest lacunarity value on the HC-T1 surface reflects the more heterogeneous topography, consistently with its higher entropy and fractal dimension. The lower lacunarity on the HC-T2 surface indicates a more regular nanotubular array.

Cell viability and proliferation

The viability and proliferation of MG63 cells were evaluated at 1-, 3- and 5-days post-seeding using the PrestoBlue assay. Fig. 2a demonstrates that cell viability on the HC surface was consistently higher at day 3 and day 5. This increased viability suggests a more favorable environment for cellular metabolism and proliferation, potentially due to its more complex nanotopography and increasing entropy and disorder which favour initial process of the cellular colonization of surfaces, such as adhesion and spreading. Fig. 2b shows a neutral response with a statistically similar total expressions of Ki-67, a well-established marker for proliferation. However, when looking at the Ki-67 positive cell counts in Fig. 2c, an intriguing finding emerges: the NT surface has a higher number of Ki-67 positive cells, despite the similar overall expression. Fig. 2d offers insight into this apparent contradiction by showing an increase in nuclear density on the HC surface. This suggests that cells on the HC surface may enter a quiescent or differentiated state more readily as they reach confluence, a phenomenon often observed in more complex topographical environments where cell–cell interactions and contact inhibition become more prominent.[17,57] Taken together, the higher cell viability and nuclear density on the HC surface suggest that the increased surface complexity provides an environment conducive to enhanced cellular metabolism and growth. This is consistent

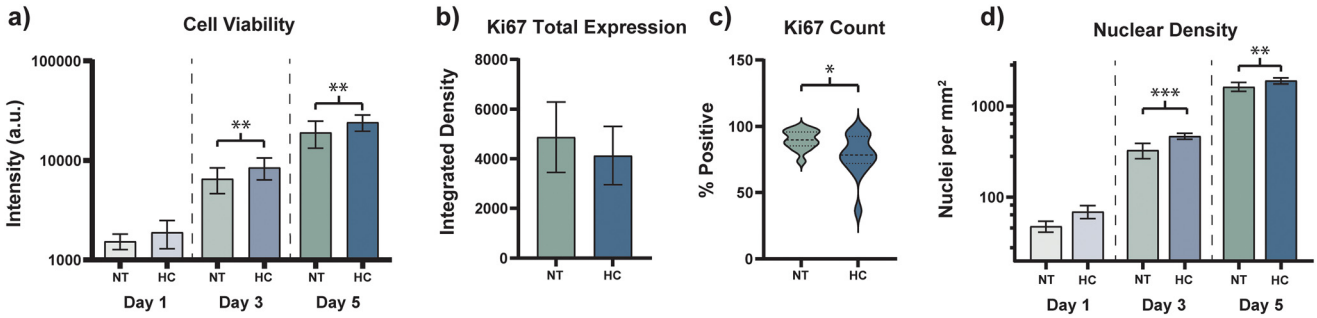

Fig. 2 Viability and proliferation of MG63 cells on NT and HC surfaces. a) PrestoBlue data measured at day 1, 3 and 5. b) Total Ki-67 expression and c) Ki-67 positivity. d) Comparison of nuclear density.

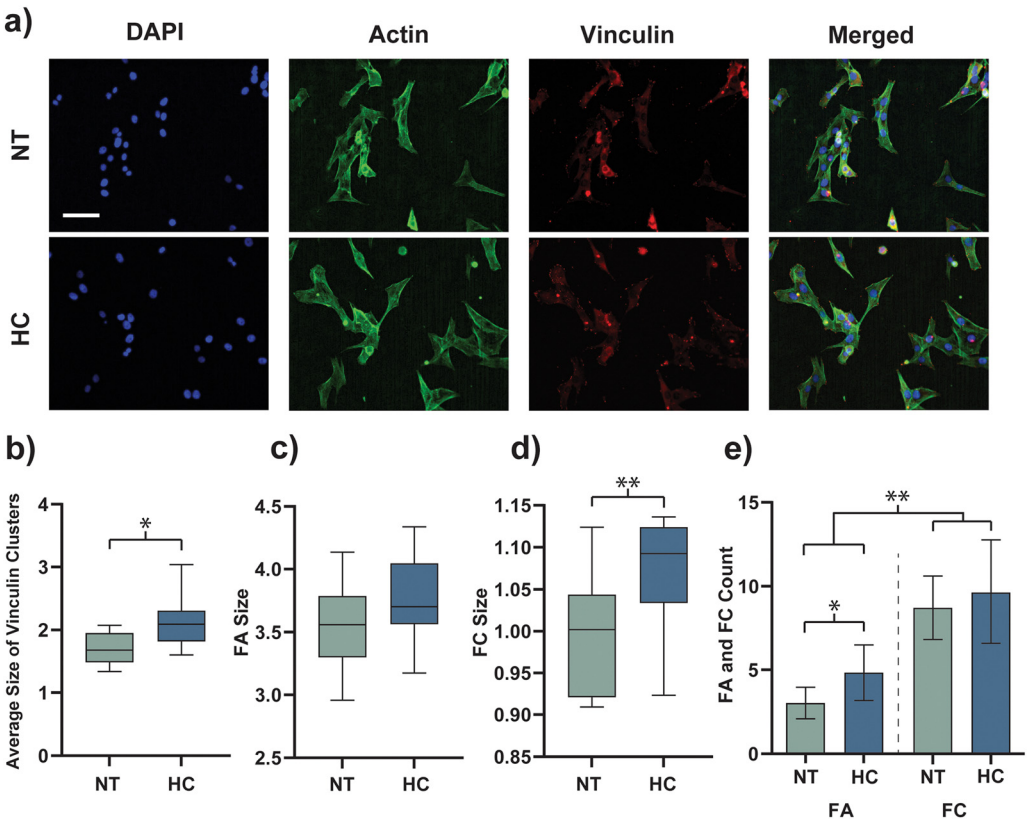

Fig. 3 Analysis of focal adhesions and complexes on NT and HC surfaces. a) Immunofluorescence images of MG63 cells. Scale bar: 100 μm. b) Average size of focal adhesions. Vinculin clusters are classified into c) focal adhesions (2–10 μm) and d) focal complexes (<2 μm). e) Focal adhesion and focal complex count after one day of attachment.

with previous studies that showed complex nanotopographies can enhance cell attachment/spreading[53,58–60] and subsequent proliferation by providing a more stimulatory environment.[53,58,60–64]

Cell adhesion

The comparative analysis of focal adhesions (FA) formation and vinculin expression reveals significant differences in cellular adhesion dynamics, crucial for understanding how these nanotopographical features influence cell behavior.[50–52] Fig. 3a displays immunofluorescence images of MG63 cells on the NT and HC surfaces on day 1-post seeding, highlighting that both surfaces successfully form vinculin-based adhesions. In particular, quantitative analysis in Fig. 3b shows that the average size of FAs on the HC surface is significantly greater than that associated with cells adhering onto the NT surface, indicating that the former better support the formation of more substantial and potentially more stable adhesions. However, when focal adhesions are broken down into specific size categories, Fig. 3c shows no significant difference in the size of mature FAs (2–10 μm).[50,52] In contrast, Fig. 3d highlights a notable difference in the smaller, transient structures known as focal

complexes (FCs) (<2 μm),[50,52] with the HC surface promoting the formation of larger FCs. The smaller FC sizes observed on the NT surface suggest an adhesion dynamic where the early stages of focal adhesion formation may be less robust. This could indicate, due to vinculin's pivotal role in FA/FC assembly and mechanotransduction, a less stable adhesion state which may potentially impact how cells perceive and respond to the substrate, negatively influencing various aspects of cell behavior, including spreading.[50–52,54,58,59] This suggests that while both surfaces support FA formation, the HC architecture encourages the maturation of FCs into more stable FAs. This is further supported by Fig. 3e which reveals that the HC surface elicits a higher number of FAs overall compared to the NT surface, thereby underscoring its potential to foster a more stable and mature adhesion environment. Notably, FC counts were significantly higher than FA counts on both surfaces. The HC surface demonstrates a clear advantage in promoting stable cell adhesion, as evidenced by the larger and more numerous FAs and FCs. These differences in adhesion dynamics may set the stage for distinct downstream signaling responses, as explored in the following section focused on the analysis of the YAP1/Hippo pathway.[65,66]

YAP1 and active YAP1

The analysis of the YAP1/Hippo signaling pathway activation on the NT and HC surfaces derives from the crucial role of mechanotransduction in the cellular response to nanotopographies. In fact, recent research has highlighted the roles of yes-associated protein 1 (YAP1) and transcriptional coactivator with PDZ-binding motif (TAZ) in mechanotransduction.[65] These proteins respond to mechanical cues and regulate cell proliferation and differentiation through the Hippo signaling pathway.[65,67] The activation of YAP1/TAZ is influenced by cytoskeletal tension and actomyosin contractility, which are modulated by substrate topography. The activation of YAP1, governed by mechanical cues, involves its translocation into the nucleus where it drives gene expression changes essential for cellular proliferation and differentiation.[65,67] This link between mechanical stimuli and YAP1 activation is particularly relevant in the context of nanotopography, where the physical features of the substrate can profoundly impact cell behavior. For this reason, various studies have assessed the significant role YAP1 activation plays in osteoblastic response to nanotubular titanium surfaces.[24,68–71]

Immunofluorescence images in Fig. 4a display YAP1 (active YAP1) and its phosphorylated form, pYAP1 (YAP1). The nuclear translocation of YAP1, a key transcriptional coactivator in the Hippo pathway, indicates that cells are responding to the mechanical cues provided by the underlying nanotopography.[65,66,72] Elevated levels of nuclear expression of active YAP1 can be observed in cells on the HC surface. Quantitative analysis (Fig. 4b) reveals that total YAP1 expression within the cell nuclei is higher on the HC

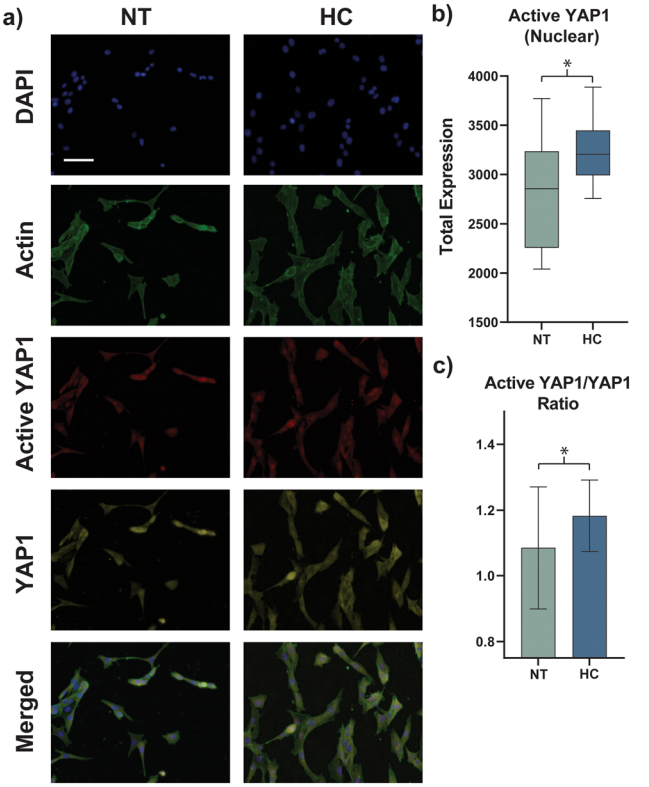

Fig. 4 Immunofluorescence images of a) actin, active YAP1 and YAP1, highlighting their localization within MG63 cells on NT and HC surfaces. Scale bar: 100 μm. b) Total YAP1 expression within cell nuclei and c) average nuclear intensity of active YAP1 to the cytoplasmic intensity of YAP1.

architecture compared to the NT surface. This elevated nuclear YAP1 expression may be a result of a stronger stimulus for early YAP1 activation by day 1. The increased focal adhesion size observed on the HC surface likely contributes to this enhancement. Large, stable focal adhesions are in fact known to influence the YAP1 pathway by altering cytoskeletal tension and cell contractility, thereby promoting YAP1 nuclear localization.[66,73–75] The correlation between increased focal adhesion size and higher nuclear active YAP1 levels reinforces the hypothesis that the HC surface promotes a more robust mechanotransductive response by the MG63 cells.[65,66]

Comparing the average intensity of active YAP1 in the cell nuclei to YAP1 in the cytoplasm (Fig. 4c) shows a higher nuclear active YAP1 intensity and lower cytoplasmic phosphorylated YAP1 in cells on the HC surface. In turn, this suggests the cells are in a state of heightened mechanotransductive activity, which could accelerate processes such as differentiation and proliferation,[57,65,66,72,73] as supported by the elevated proliferative levels (Fig. 2). Taken together, this trend indicates that the HC surface is more effective at promoting early cellular differentiation (as demonstrated in Fig. 5), adding to the body of literature highlighting YAP1's impact on osteoblast differentiation.[24,68–71]

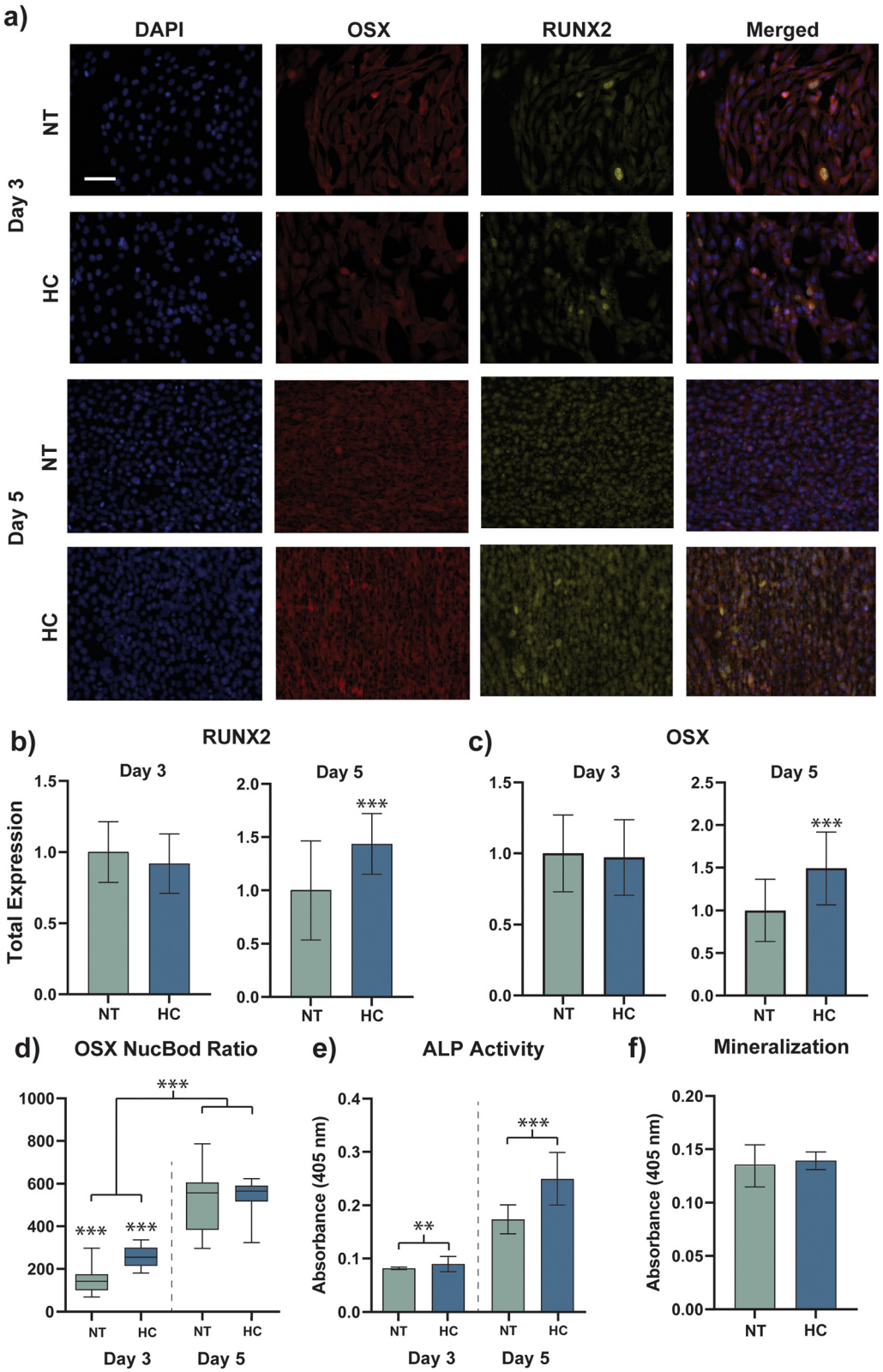

Fig. 5 Immunofluorescence images of a) RUNX2 and OSX at day 3 and day 5. Scale bar: 100 μm. Normalized (against the NT surface) expression of b) nuclear RUNX2 and c) OSX at day 3 and day 5. d) Nuclear-to-cytoplasmic OSX expression ratio at day 3. e) ALP activity at day 3 and day 5. f) Alizarin red assay (mineralization) after 21 days of culture.

Differentiation

The expression of the osteogenic markers RUNX2 and OSX, along with the ALP activity and mineralization, were evaluated to assess surface-driven osteogenic differentiation. Immunofluorescence images of RUNX2 and OSX at day 3 and day 5 (Fig. 5a) qualitatively indicate a higher expression of these markers in cells on the HC surface. Quantitative analysis at day 3 shows no significant difference in RUNX2 and OSX total expression within the nucleus (Fig. 5b). However, at day 5, a significant increase in nuclear expression of both RUNX2 and OSX is observed on the HC surface (Fig. 5c). Further analysis reveals that the ratio of nuclear to cytoplasmic OSX expression at day 3 is more elevated on the HC surface (Fig. 5d). This early surge in OSX expression, followed by its rapid translocation to the nucleus,[76,77] supports the notion that the HC surface induces a quicker initiation of the differentiation process. By day 5, however, this early advantage normalizes, indicating that the cells on the HC surface may reach a differentiated state more rapidly than those on the NT surface. This differentiation trend is further corroborated by ALP data, where significantly higher activity is detected at both day 3 and day 5 on the HC surface (Fig. 5e). Interestingly, despite the accelerated differentiation observed on the HC surface, mineralization shows no distinguishable difference between the two surfaces after 21 days (Fig. 5f).

These results provide evidence that the HC surface promotes a more rapid onset of osteogenic differentiation in MG63 cells compared to the NT surface. RUNX2 and OSX are in fact critical transcription factors in the osteogenic pathway, with RUNX2 initiating the differentiation process and OSX being essential for the maturation of pre-osteoblasts into fully functional osteoblast.[76–79] The significant increase in the nuclear expression by day 5 on the HC surface of these key transcription factors[55,78,80,81] indicate that the HC nanotopography is highly effective in driving early osteogenic differentiation, likely due to the increased propensity to form large, stable focal adhesions (Fig. 3) and the enhanced mechanotransductive signaling observed in earlier YAP pathway activation (Fig. 4). Notably, the elevated nuclear-to-cytoplasmic ratio of OSX at day 3 on the HC surface further underscores the early onset of differentiation. This early nuclear localization is indicative of a rapid transition from a proliferative to a differentiated state, which is consistent with the observed increase in ALP activity. ALP is a key enzyme involved in the early stages of mineralization, and its higher activity on the HC surface suggests that cells are not only differentiating more quickly but are also preparing for the mineralization phase of bone formation. However, the lack of difference in mineral deposition between the two surfaces after 21 days raises interesting questions about the long-term effects of early differentiation. While the HC surface clearly promotes rapid osteoinduction, this does not necessarily lead to a greater accumulation of mineralized matrix over time. This finding indicates that while early differentiation markers may be upregulated, the ultimate amount of mineralization may be influenced by other factors, ultimately highlighting the importance of considering both early and late-stage markers in the design and evaluation of biomaterials intended for bone regeneration.

Mineral quality

Raman spectroscopy was employed to assess and compare the quality of mineral deposits on these surfaces, a critical aspect given that alizarin assay results were statistically similar for the two surfaces analyzed in this work (Fig. 5f).

We assessed the composition of the mineralized deposits formed by MG63 cells after 21 days of culture.[82,83] The

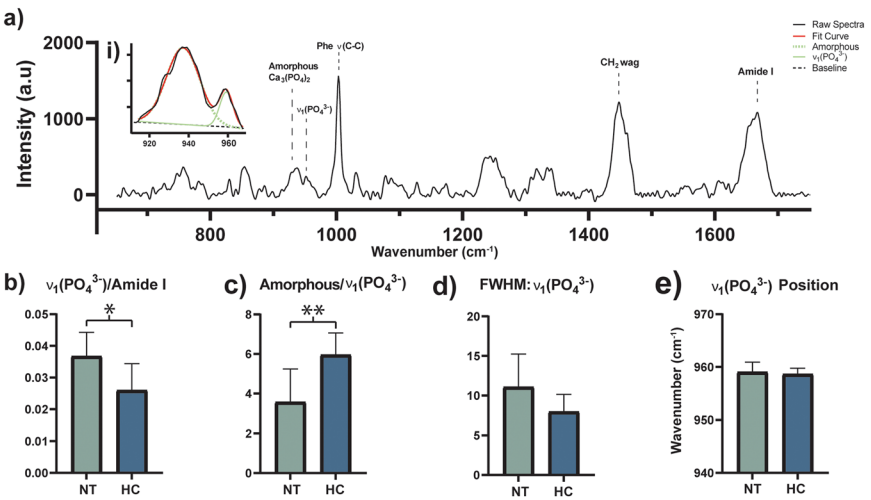

Fig. 6 Raman analysis of mineralization on NT and HC surfaces after 21 days in culture. a) Representative Raman spectra of the small mineral deposits, with nested panel i) demonstrating peak deconvolution between the 960 cm^{-1} (calcium phosphate) and 940 cm^{-1} (amorphous calcium phosphate) peaks. Mineral composition analysis compared *via* b) $\nu_1(PO_4^{3-})$/amide I ratio, c) amorphous calcium phosphate/$\nu_1(PO_4^{3-})$, d) FWHM (of $\nu_1(PO_4^{3-})$ peak), and e) the position of the $\nu_1(PO_4^{3-})$ peak.

representative Raman spectrum of the mineral formations showcases distinct peaks associated with crystalline hydroxyapatite and with amorphous calcium phosphate (Fig. 6a). A significantly higher $\nu_1(PO_4^{3-})$/amide I ratio was observed in deposits deriving from the cellular activity on the NT surface (Fig. 6b), indicating a greater presence of crystalline hydroxyapatite. In contrast, formations on the HC surface exhibited a higher amorphous calcium phosphate to crystalline hydroxyapatite ratio (Fig. 6c), indicating that the mineralization on this surface is less advanced. Interestingly, no significant differences were observed in terms of the full width at half maximum (FWHM) of the phosphate peak and the position of the phosphate peak at 960 cm^{-1} (Fig. 6d), indicating that the crystallinity of the mineral formed on both surfaces was comparable.[30,84,85] Taken together, our results show that the NT surface appears to facilitate more advanced mineralization, as indicated by the higher $\nu_1(PO_4^{3-})$/amide I ratio, which reflects a greater presence of crystalline hydroxyapatite. In parallel, the HC surface shows a higher proportion of amorphous calcium phosphate relative to crystalline hydroxyapatite, implying that mineralization on this surface is still in a less mature phase.[86,87] It should also be noted that MG63 cells are known for their lack of production of high quality bone mineral in comparison to other immortalized osteoblastic cell lines.[88] This does not invalidate the comparative results; however, it may explain the lack of an intense and sharp $\nu_1(PO_4^{3-})$ peak along with the early 21 day timepoint. These results provide context to the alizarin results, offering a better understanding of mineralization process between these two osteogenic surfaces, slightly favoring the NT surface for long term production of mineral.

Conclusion

This study demonstrates that the HC surface markedly enhances early cellular response, most notably by accelerating proliferation and promoting early osteogenic differentiation in MG63 cells. The observed increase in cell viability, coupled with the pronounced upregulation of early differentiation markers, establishes the HC surface as a substrate capable of fostering more rapid cellular attachment and growth. These results highlight the critical role of nanotopographical complexity in modulating cell behavior, positioning the HC surface as a promising candidate for applications demanding swift cell proliferation and differentiation. Furthermore, the significantly elevated number of focal adhesions (FAs) on the HC surface compared to the NT surface underscores its enhanced capacity to support robust and mature cell adhesion—an essential prerequisite for effective mechanotransduction and the activation of downstream signaling pathways. The heightened nuclear localization of YAP1 provides evidence that mechanotransduction is a pivotal driver of the enhanced cellular responses observed on the HC surface. However, despite the HC surface's clear advantages in early cellular dynamics, the NT single-tube surface drives mineralization that rivals the HC surface, as evidenced by the alizarin assay. Notably, the NT surface yields mineral deposits of superior quality, distinguished by a greater abundance of crystalline hydroxyapatite—a critical factor for ensuring long-term bone stability and structural integrity. This suggests that while the HC surface excels in eliciting early cellular activity, the NT surface demonstrates greater efficacy in fostering the formation of mature mineral deposits. Taken together, these findings highlight a complementary relationship between the two architectures: the HC surface could be viewed as a closer analogue to the heterogeneous extracellular matrix, which may explain its capacity to foster early cellular activity, whereas the NT reflects a more uniform template conducive to mineral stability. In light of this distinction, the selective strengths of the HC and NT surfaces suggest potential application-specific deployment: HC-like surfaces could be leveraged for rapid osseointegration in conditions where early stability is critical, whereas NT-like architectures may be preferable in load-bearing implants requiring durable interfacial mineral formation. Looking ahead, future implant surfaces may achieve the best of both approaches through hybrid or gradient designs that mirror the staged biology of bone healing by initiating early cellular recruitment and differentiation, followed by the formation of high-quality mineralized tissue.

Beyond these biological and materials considerations, the practical implementation of the NT or HC architecture requires careful attention to manufacturing scalability. While our results and prior work demonstrate that these nanostructures can be generated with excellent reproducibility through anodization, translating this process to industrial-scale production raises additional considerations. Specifically, maintaining consistent nanotopographical features across large implant surfaces will require robust process control and monitoring, particularly as implant geometries become more complex. Cost-effectiveness is another critical factor, as multi-step anodization must be optimized to minimize production time without compromising surface quality. At scale, integration with automated fabrication lines and standardized quality assurance methods will be essential to ensure batch-to-batch consistency and regulatory compliance. Addressing these technical and economic aspects will be key to bridging the gap between the demonstrated biological advantages of the NT and HC architectures and their adoption in clinically deployable implant technologies.

In parallel with these translational considerations, it is also important to consider the broader methodological implications of this work. Although anodization is particularly suited to Ti, other fabrication strategies (*e.g.*, laser texturing, plasma deposition, chemical etching) can also introduce varying degrees of topographical disorder on biomedically relevant metals and alloys, for which metrics such as entropy, lacunarity and fractal dimension will capture the hierarchical complexity of nanoscale organization by extending beyond

conventional geometric descriptors. This quantitative framework is poised to transform disorder from an incidental outcome of fabrication into a deliberate design parameter, enabling rigorous correlation with cell adhesion, proliferation and differentiation across diverse material systems. By embedding spatial statistical analysis into biomaterials research, disorder can be reframed as a biologically meaningful and controllable variable, offering a unifying principle that transcends specific materials or processing methods. In this way, disorder emerges as a versatile and broadly applicable tool to guide the rational development of next-generation implant surfaces that promote robust tissue integration and long-term functionality.

In conclusion, this research advances our understanding of how nanotopographical features govern MG63 cell behavior. More broadly, this work illustrates how integrating spatial analyses into surface evaluation reframes disorder from a fabrication byproduct into a controllable, biologically meaningful variable. Together, these insights provide guidance for the rational design of next-generation implant surfaces that combine biological efficacy with practical manufacturability, ultimately advancing the development of multifunctional cell-instructive surfaces.

Conflicts of interest

There are no conflicts to declare.

Data availability

The data that support the findings of this study are available from the corresponding author upon reasonable request.

Acknowledgements

The authors acknowledge financial support from the Natural Sciences and Engineering Research Council of Canada (NSERC) through the Discovery Grant program, Canada Foundation for Innovation (CFI) and the Ontario Ministry of Research and Innovation (MRI) through the Leaders of Opportunity (LOF) fund. R. B. expresses appreciation to NSERC for funding provided by the Canada Graduate Scholarship. The authors also extend their gratitude to the Cell Biology and Image Acquisition (CBIA) Core Facility for providing access to fluorescence microscopes and to Chloë Van Oostende-Triplet and Liyuan Wang for their technical support and guidance in microscopy.

References

1 P. Kazimierczak and A. Przekora, Osteoconductive and Osteoinductive Surface Modifications of Biomaterials for Bone Regeneration: A Concise Review, *Coatings*, 2020, **10**, 971, DOI: **10.3390/coatings10100971**.

2 X. Yan, W. Cao and H. Li, Biomedical alloys and physical surface modifications: A mini-review, *Materials*, 2022, **15**, 66–82, DOI: **10.3390/ma15010066**.

3 S. Dobbenga, L. E. Fratila-Apachitei and A. A. Zadpoor, Nanopattern-induced osteogenic differentiation of stem cells – A systematic review, *Acta Biomater.*, 2016, **46**, 3–14, DOI: **10.1016/j.actbio.2016.09.031**.

4 M. Saini, Implant biomaterials: A comprehensive review, *World J. Clin. Cases*, 2015, **3**(1), 52, DOI: **10.12998/wjcc.v3.i1.52**.

5 D. Karazisis, L. Rasmusson and S. Petronis, *et al.*, The effects of controlled nanotopography, machined topography and their combination on molecular activities, bone formation and biomechanical stability during osseointegration, *Acta Biomater.*, 2021, **136**, 279–290, DOI: **10.1016/j.actbio.2021.10.001**.

6 F. Mastrangelo, R. Quaresima, L. Canullo, A. Scarano, L. Muzio and A. Piattelli, Effects of Novel Laser Dental Implant Microtopography on Human Osteoblast Proliferation and Bone Deposition, *Int. J. Oral Maxillofac. Implants*, 2020, **35**(2), 320–329, DOI: **10.11607/jomi.7606**.

7 A. Barlian and K. Vanya, Nanotopography in directing osteogenic differentiation of mesenchymal stem cells: Potency and future perspective, *Future Sci. OA*, 2022, **8**, 1–15, DOI: **10.2144/fsoa-2021-0097**.

8 R. L. Bighetti-Trevisan, E. P. Ferraz and M. B. F. Silva, *et al.*, Effect of osteoblasts on osteoclast differentiation and activity induced by titanium with nanotopography, *Colloids Surf., B*, 2023, **229**, 113448, DOI: **10.1016/j.colsurfb.2023.113448**.

9 P. G. Souza, L. F. Adolpho and H. B. Lopes, *et al.*, Effects of Modulation of the Hedgehog and Notch Signaling Pathways on Osteoblast Differentiation Induced by Titanium with Nanotopography, *J. Funct. Biomater.*, 2023, **14**, 79, DOI: **10.3390/jfb14020079**.

10 C. Hou, J. An and D. Zhao, *et al.*, Surface Modification Techniques to Produce Micro/Nano-scale Topographies on Ti-Based Implant Surfaces for Improved Osseointegration, *Front. Bioeng. Biotechnol.*, 2022, **10**, 1–16, DOI: **10.3389/fbioe.2022.835008**.

11 Y. Zhang, Z. Fan, Y. Xing, S. Jia, Z. Mo and H. Gong, Effect of microtopography on osseointegration of implantable biomaterials and its modification strategies, *Front. Bioeng. Biotechnol.*, 2022, **10**, 1–14, DOI: **10.3389/fbioe.2022.981062**.

12 M. Petrini, T. V. Pierfelice and E. D'amico, *et al.*, Influence of nano, micro and macro topography of dental implant surfaces on human gingival fibroblasts, *Int. J. Mol. Sci.*, 2021, **22**, 9871, DOI: **10.3390/ijms22189871**.

13 J. Luo, S. Zhao and X. Gao, *et al.*, TiO2 Nanotopography-Driven Osteoblast Adhesion through Coulomb's Force Evolution, *ACS Appl. Mater. Interfaces*, 2022, **14**(30), 34400–34414, DOI: **10.1021/acsami.2c07652**.

14 A. I. M. Greer, V. Goriainov and J. Kanczler, *et al.*, Nanopatterned Titanium Implants Accelerate Bone Formation in Vivo, *ACS Appl. Mater. Interfaces*, 2020, **12**(30), 33541–33549, DOI: **10.1021/acsami.0c10273**.

15 E. Huethorst, M. F. A. Cutiongco and F. A. Campbell, *et al.*, Customizable, engineered substrates for rapid screening of cellular cues, *Biofabrication*, 2020, **12**, 025009, DOI: **10.1088/1758-5090/ab5d3f**.

16 R. Cuahtecontzi Delint, M. I. Ishak and P. M. Tsimbouri, *et al.*, Nanotopography Influences Host-Pathogen Quorum Sensing and Facilitates Selection of Bioactive Metabolites in Mesenchymal Stromal Cells and Pseudomonas aeruginosa Co-Cultures, *ACS Appl. Mater. Interfaces*, 2024, **16**, 43374–43386, DOI: **10.1021/acsami.4c09291**.

17 J. Luo, M. Walker, Y. Xiao, H. Donnelly, M. J. Dalby and M. Salmeron-Sanchez, The influence of nanotopography on cell behaviour through interactions with the extracellular matrix – A review, *Bioact. Mater.*, 2022, **15**, 145–159, DOI: **10.1016/j.bioactmat.2021.11.024**.

18 R. M. Visalakshan, A. A. Cavallaro and M. N. MacGregor, *et al.*, Nanotopography-Induced Unfolding of Fibrinogen Modulates Leukocyte Binding and Activation, *Adv. Funct. Mater.*, 2019, **29**, 1807453, DOI: **10.1002/adfm.201807453**.

19 A. Bachhuka, B. Delalat, S. R. Ghaemi, S. Gronthos, N. H. Voelcker and K. Vasilev, Nanotopography mediated osteogenic differentiation of human dental pulp derived stem cells, *Nanoscale*, 2017, **9**(37), 14248–14258, DOI: **10.1039/c7nr03131a**.

20 R. V. Goreham, A. Mierczynska, L. E. Smith, R. Sedev and K. Vasilev, Small surface nanotopography encourages fibroblast and osteoblast cell adhesion, *RSC Adv.*, 2013, **3**(26), 10309–10317, DOI: **10.1039/c3ra23193c**.

21 A. K. Rajendran, D. Sankar, S. Amirthalingam, H. D. Kim, J. Rangasamy and N. S. Hwang, Trends in mechanobiology guided tissue engineering and tools to study cell-substrate interactions: a brief review, *Biomater. Res.*, 2023, **27**(1), 1–24, DOI: **10.1186/s40824-023-00393-8**.

22 Y. Zhang, K. Li and G. Li, *et al.*, Investigation of nanotopography on SOCE mediated cell migration via live-cell: Imaging on opaque implant surface, *J. Nanobiotechnol.*, 2023, **21**(1), 1–12, DOI: **10.1186/s12951-023-02249-8**.

23 C. W. Kuo, D. Y. Chueh and P. Chen, Investigation of size-dependent cell adhesion on nanostructured interfaces, *J. Nanobiotechnol.*, 2014, **12**(1), 1–10, DOI: **10.1186/s12951-014-0054-4**.

24 R. Cuahtecontzi Delint, H. Jaffery, M. I. Ishak, A. H. Nobbs, B. Su and M. J. Dalby, Mechanotransducive surfaces for enhanced cell osteogenesis, a review, *Biomater. Adv.*, 2024, **160**, 213861, DOI: **10.1016/j.bioadv.2024.213861**.

25 K. Gulati, Y. Zhang, P. Di, Y. Liu and S. Ivanovski, Research to Clinics: Clinical Translation Considerations for Anodized Nano-Engineered Titanium Implants, *ACS Biomater. Sci. Eng.*, 2022, **8**(10), 4077–4091, DOI: **10.1021/acsbiomaterials.1c00529**.

26 D. Chopra, K. Gulati and S. Ivanovski, Understanding and optimizing the antibacterial functions of anodized nano-engineered titanium implants, *Acta Biomater.*, 2021, **127**, 80–101, DOI: **10.1016/j.actbio.2021.03.027**.

27 R. Fan and J. Wan, Electrode distance regulates the anodic growth of titanium dioxide (TiO2) nanotubes, *Nanotechnology*, 2017, **28**, 25LT01, DOI: **10.1088/1361-6528/aa703d**.

28 J. Park, A. B. Tesler, E. Gongadze, A. Iglic, P. Schmuki and A. Mazare, Nanoscale Topography of Anodic TiO 2 Nanostructures Is Crucial for Cell – Surface Interactions, *ACS Appl. Mater. Interfaces*, 2024, **16**, 4430–4438, DOI: **10.1021/acsami.3c16033**.

29 S. A. Batool, M. Salman Maqbool, M. A. Javed, A. Niaz and M. A. U. Rehman, A Review on the Fabrication and Characterization of Titania Nanotubes Obtained via Electrochemical Anodization, *Surfaces*, 2022, **5**(4), 456–480, DOI: **10.3390/surfaces5040033**.

30 A. J. Steeves, W. Ho and M. C. Munisso, *et al.*, The implication of spatial statistics in human mesenchymal stem cell response to nanotubular architectures, *Int. J. Nanomed.*, 2020, **15**, 2151–2169, DOI: **10.2147/IJN.S238280**.

31 R. Berthelot and F. Variola, Investigating the interplay between environmental conditioning and nanotopographical cueing on the response of human MG63 osteoblastic cells to titanium nanotubes, *Biomater. Sci.*, 2025, **13**, 946–968, DOI: **10.1039/D4BM00792A**.

32 S. Di Cio and J. E. Gautrot, Cell sensing of physical properties at the nanoscale: Mechanisms and control of cell adhesion and phenotype, *Acta Biomater.*, 2016, **30**, 26–48, DOI: **10.1016/j.actbio.2015.11.027**.

33 I. Wheeldon, A. Farhadi, A. G. Bick, E. Jabbari and A. Khademhosseini, Nanoscale tissue engineering: Spatial control over cell-materials interactions, *Nanotechnology*, 2011, **22**, 212001, DOI: **10.1088/0957-4484/22/21/212001**.

34 M. J. P. Biggs and L. E. McNamara, The modulation of skeletal stem cell function through nanoscale topography, *Stem Cells and Bone Tissue*, 2013, pp. 125–144, DOI: **10.1201/b14590**.

35 N. I. Aminuddin, R. Ahmad, S. A. Akbar and B. Pingguan-Murphy, Osteoblast and stem cell response to nanoscale topographies: a review, *Sci. Technol. Adv. Mater.*, 2016, **17**(1), 698–714, DOI: **10.1080/14686996.2016.1242999**.

36 Y. Zhang, A. Gordon, W. Qian and W. Chen, Engineering Nanoscale Stem Cell Niche: Direct Stem Cell Behavior at Cell-Matrix Interface, *Adv. Healthcare Mater.*, 2015, **4**(13), 1900–1914, DOI: **10.1002/adhm.201500351**.

37 G. M. de Peppo, H. Agheli and C. Karlsson, *et al.*, Osteogenic response of human mesenchymal stem cells to well-defined nanoscale topography in vitro, *Int. J. Nanomed.*, 2014, **9**(1), 2499–2515, DOI: **10.2147/IJN.S58805**.

38 Z. Xu, J. Huang, Y. He, J. Su, L. Xu and X. Zeng, Fabrication of an ordered micro-/nanotextured titanium surface to improve osseointegration, *Colloids Surf., B*, 2022, **214**, 112446, DOI: **10.1016/j.colsurfb.2022.112446**.

39 K. S. Brammer, S. Oh, C. J. Cobb, L. M. Bjursten, H. van der Heyde and S. Jin, Improved bone-forming functionality on diameter-controlled TiO2 nanotube surface, *Acta Biomater.*, 2009, **5**(8), 3215–3223, DOI: **10.1016/j.actbio.2009.05.008**.

40 S. Oh, K. S. Brammer and Y. S. J. Li, Stem cell fate dictated solely by altered nanotube dimension, *Proc. Natl. Acad. Sci. U. S. A.*, 2009, **106**, 2130–2135, DOI: **10.1073/pnas.0813200106**.

41 H. Tang, Y. Li and J. Ma, *et al.*, Improvement of biological and mechanical properties of titanium surface by anodic oxidation, *Biomed. Mater. Eng.*, 2016, **27**(5), 485–494, DOI: **10.3233/BME-161602**.

42 J. Schindelin, I. Arganda-Carreras and E. Frise, *et al.*, Fiji: An open-source platform for biological-image analysis, *Nat. Methods*, 2012, **9**(7), 676–682, DOI: **10.1038/nmeth.2019**.

43 A. Delgado-Bonal and A. Marshak, Approximate Entropy and Sample Entropy: A Comprehensive Tutorial, *Entropy*, 2019, **21**, 541, DOI: **10.3390/e21060541**.

44 J. S. Richman, J. Randall Moorman, J. Randall and M. Physi, Physiological time-series analysisusing approximate entropy and sample entropy, *Am. J. Physiol.*, 2000, **278**, 2039–2049, DOI: **10.1152/ajpheart.2000.278.6.H2039**.

45 L. E. V. Silva, A. C. S. S. Filho, V. P. S. Fazan, J. C. Felipe and L. O. Murta, Two-dimensional sample entropy: Assessing image texture through irregularity, *Biomed. Phys. Eng. Express*, 2016, **2**, 045002, DOI: **10.1088/2057-1976/2/4/045002**.

46 L. E. Virgilio Da Silva, A. C. Da Silva Senra Filho, V. P. S. Fazan, J. C. Felipe and L. O. Murta, Two-dimensional sample entropy analysis of rat sural nerve aging, *2014 36th Annual International Conference of the IEEE Engineering in Medicine and Biology Society, EMBC 2014*, Published online, 2014, pp. 3345–3348, DOI: **10.1109/EMBC.2014.6944339**.

47 R. Berthelot and F. Variola, Investigating the interplay between environmental conditioning and nanotopographical cueing on the response of human MG63 osteoblastic cells to titanium nanotubes, *Biomater. Sci.*, 2025, **13**, 946–968.

48 I. G. Torre, R. J. Heck and A. M. Tarquis, MULTIFRAC: An ImageJ plugin for multiscale characterization of 2D and 3D stack images, *SoftwareX*, 2020, **12**, 100574, DOI: **10.1016/j.softx.2020.100574**.

49 T. G. Smith, G. D. Lange and W. B. Marks, Fractal methods and results in cellular morphology - Dimensions, lacunarity and multifractals, *J. Neurosci. Methods*, 1996, **69**(2), 123–136, DOI: **10.1016/S0165-0270(96)00080-5**.

50 L. Xiao, M. Ding and O. Saadoon, *et al.*, A novel culture platform for fast proliferation of human annulus fibrosus cells, *Cell Tissue Res.*, 2017, **367**(2), 339–350, DOI: **10.1007/s00441-016-2497-4**.

51 C. Tolbert and K. Burridge, Focal Adhesions, *Cellular Domains*, 2011, pp. 285–302, DOI: **10.1002/9781118015759.ch17**.

52 U. Horzum, B. Ozdil and D. Pesen-Okvur, Step-by-step quantitative analysis of focal adhesions, *MethodsX*, 2014, **1**(1), 56–59, DOI: **10.1016/j.mex.2014.06.004**.

53 C. Allan, A. Ker and C. A. Smith, *et al.*, Osteoblast response to disordered nanotopography, *J. Tissue Eng.*, 2018, **9**, 1–7, DOI: **10.1177/2041731418784098**.

54 M. J. Dalby, N. Gadegaard and R. Tare, *et al.*, The control of human mesenchymal cell differentiation using nanoscale symmetry and disorder, *Nat. Mater.*, 2007, **6**(12), 997–1003, DOI: **10.1038/nmat2013**.

55 M. J. Dalby, N. Gadegaard and R. O. C. Oreffo, Harnessing nanotopography and integrin-matrix interactions to influence stem cell fate, *Nat. Mater.*, 2014, **13**(6), 558–569, DOI: **10.1038/nmat3980**.

56 R. E. Plotnick, R. H. Gardner, W. W. Hargrove, K. Prestegaard and M. Perlmutter, Lacunarity analysis: A general technique for the analysis of spatial patterns, *Phys. Rev. E: Stat. Phys., Plasmas, Fluids, Relat. Interdiscip. Top.*, 1996, **53**(5), 5461–5468, DOI: **10.1103/PhysRevE.53.5461**.

57 B. M. Gumbiner and N. G. Kim, The Hippo-YAP signaling pathway and contact inhibition of growth, *J. Cell Sci.*, 2014, **127**(4), 709–717, DOI: **10.1242/jcs.140103**.

58 X. Wang, C. Yan, K. Ye, Y. He, Z. Li and J. Ding, Effect of RGD nanospacing on differentiation of stem cells, *Biomaterials*, 2013, **34**(12), 2865–2874, DOI: **10.1016/j.biomaterials.2013.01.021**.

59 W. Xie, X. Wei and H. Kang, *et al.*, Static and Dynamic: Evolving Biomaterial Mechanical Properties to Control Cellular Mechanotransduction, *Adv. Sci.*, 2023, **10**(9), 1–37, DOI: **10.1002/advs.202204594**.

60 J. Luo, M. Walker, Y. Xiao, H. Donnelly, M. J. Dalby and M. Salmeron-Sanchez, The influence of nanotopography on cell behaviour through interactions with the extracellular matrix – A review, *Bioact. Mater.*, 2022, **15**, 145–159, DOI: **10.1016/j.bioactmat.2021.11.024**.

61 K. Anselme, A. Ponche and M. Bigerelle, Relative influence of surface topography and surface chemistry on cell response to bone implant materials. Part 2: Biological aspects, *Proc. Inst. Mech. Eng., Part H*, 2010, **224**(12), 1487–1507, DOI: **10.1243/09544119JEIM901**.

62 J. Luo, M. Walker, Y. Xiao, H. Donnelly, M. J. Dalby and M. Salmeron-Sanchez, The influence of nanotopography on cell behaviour through interactions with the extracellular matrix – A review, *Bioact. Mater.*, 2022, **15**, 145–159, DOI: **10.1016/j.bioactmat.2021.11.024**.

63 X. Chen, H. Fan and X. Deng, *et al.*, Scaffold structural microenvironmental cues to guide tissue regeneration in bone tissue applications, *Nanomaterials*, 2018, **8**(11), 1–15, DOI: **10.3390/nano8110960**.

64 S. Oh, C. Daraio, L. H. Chen, T. R. Pisanic, R. R. Fiñones and S. Jin, Significantly accelerated osteoblast cell growth on aligned TiO2 nanotubes, *J. Biomed. Mater. Res., Part A*, 2006, **78**(1), 97–103, DOI: **10.1002/jbm.a.30722**.

65 V. Arvind and A. H. Huang, Mechanobiology of limb musculoskeletal development, *Ann. N. Y. Acad. Sci.*, 2017, **1409**(1), 18–32, DOI: **10.1111/nyas.13427**.

66 S. Dupont, L. Morsut and M. Aragona, *et al.*, Role of YAP/TAZ in mechanotransduction, *Nature*, 2011, **474**(7350), 179–184, DOI: **10.1038/nature10137**.

67 P. Tsimbouri, Adult Stem Cell Responses to Nanostimuli, *J. Funct. Biomater.*, 2015, **6**(3), 598–622, DOI: **10.3390/jfb6030598**.

68 Y. Sun, Y. Yu and S. Ma, *et al.*, Nanotube topography rejuvenates the senescence of mesenchymal stem cells by activating YAP signalling, *J. Mater. Chem. B*, 2024, **12**(28), 6917–6926, DOI: **10.1039/d3tb02828c**.

69 Z. Tong, Y. Liu and R. Xia, *et al.*, F-actin Regulates Osteoblastic Differentiation of Mesenchymal Stem Cells on TiO2 Nanotubes Through MKL1 and YAP/TAZ, *Nanoscale Res. Lett.*, 2020, **15**, 183, DOI: **10.1186/s11671-020-03415-9**.

70 H. Zhang, L. F. Cooper and X. Zhang, *et al.*, Titanium nanotubes induce osteogenic differentiation through the

FAK/RhoA/YAP cascade, *RSC Adv.*, 2016, **6**(50), 44062–44069, DOI: **10.1039/c6ra04002k**.

71 L. Li, S. Yang and L. Xu, *et al.*, Nanotopography on titanium promotes osteogenesis via autophagy-mediated signaling between YAP and β-catenin, *Acta Biomater.*, 2019, **96**, 674–685, DOI: **10.1016/j.actbio.2019.07.007**.

72 K. Kong, Y. Chang and Y. Hu, *et al.*, TiO2 Nanotubes Promote Osteogenic Differentiation Through Regulation of Yap and Piezo1, *Front. Bioeng. Biotechnol.*, 2022, **10**, 1–13, DOI: **10.3389/fbioe.2022.872088**.

73 M. Aragona, T. Panciera and A. Manfrin, *et al.*, A mechanical checkpoint controls multicellular growth through YAP/TAZ regulation by actin-processing factors, *Cell*, 2013, **154**(5), 1047–1059, DOI: **10.1016/j.cell.2013.07.042**.

74 Y. Zhang, M. M. P. Zegers, A. Nagelkerke, A. E. Rowan, P. N. Span and P. H. J. Kouwer, Tunable Hybrid Matrices Drive Epithelial Morphogenesis and YAP Translocation, *Adv. Sci.*, 2021, **8**(2), 1–16, DOI: **10.1002/advs.202003380**.

75 J. E. Sero and C. Bakal, Multiparametric Analysis of Cell Shape Demonstrates that β-PIX Directly Couples YAP Activation to Extracellular Matrix Adhesion, *Cell Syst.*, 2017, **4**(1), 84–96.E6, DOI: **10.1016/j.cels.2016.11.015**.

76 G. Yang, G. Yuan, M. MacDougall, C. Zhi and S. Chen, BMP-2 induced Dspp transcription is mediated by Dlx3/Osx signaling pathway in odontoblasts, *Sci. Rep.*, 2017, **7**(1), 1–11, DOI: **10.1038/s41598-017-10908-8**.

77 G. Tai, I. Christodoulou, A. E. Bishop and J. M. Polak, Use of green fluorescent fusion protein to track activation of the transcription factor osterix during early osteoblast differentiation, *Biochem. Biophys. Res. Commun.*, 2005, **333**(4), 1116–1122, DOI: **10.1016/j.bbrc.2005.05.195**.

78 M. J. Davison, R. J. McMurray, C. A. Smith, M. J. Dalby and R. D. Meek, Nanopit-induced osteoprogenitor cell differentiation: The effect of nanopit depth, *J. Tissue Eng.*, 2016, **7**, 1–8, DOI: **10.1177/2041731416652778**.

79 H. Jiang, X. Ma and W. Zhou, *et al.*, The Effects of Hierarchical Micro/Nano-Structured Titanium Surface on Osteoblast Proliferation and Differentiation under Diabetic Conditions, *Implant Dent.*, 2017, **26**(2), 263–269, DOI: **10.1097/ID.0000000000000576**.

80 Y. T. Tsao, Y. J. Huang, H. H. Wu, Y. A. Liu, Y. S. Liu and O. K. Lee, Osteocalcin mediates biomineralization during osteogenic maturation in human mesenchymal stromal cells, *Int. J. Mol. Sci.*, 2017, **18**, 159, DOI: **10.3390/ijms18010159**.

81 E. H. Burger, J. Klein-Nulend and S. C. Cowin, Mechanotransduction in Bone, in *Molecular and Cellular Biology of Bone*, Advances in Organ Biology, Elsevier, 1998, vol. 5, pp. 123–136, DOI: **10.1016/S1569-2590(08)60110-X**.

82 Y. J. Hong, J. S. Chun and W. K. Lee, Association of collagen with calcium phosphate promoted osteogenic responses of osteoblast-like MG63 cells, *Colloids Surf., B*, 2011, **83**(2), 245–253, DOI: **10.1016/j.colsurfb.2010.11.028**.

83 Y. S. Choi, Y. J. Hong and J. Hur, *et al.*, Bone nodule formation of MG63 cells is increased by the interplay of signaling pathways cultured on vitamin D3-entrapped calcium phosphate films, *Anim. Cells Syst.*, 2009, **13**(4), 363–370, DOI: **10.1080/19768354.2009.9647231**.

84 M. Unal, R. Ahmed, A. Mahadevan-Jansen and J. S. Nyman, Compositional assessment of bone by Raman spectroscopy, *Analyst*, 2021, **146**(24), 7444–7470, DOI: **10.1039/d1an01560e**.

85 F. A. Shah, Towards refining Raman spectroscopy-based assessment of bone composition, *Sci. Rep.*, 2020, **10**(1), 1–8, DOI: **10.1038/s41598-020-73559-2**.

86 J. A. Stammeier, B. Purgstaller, D. Hippler, V. Mavromatis and M. Dietzel, In-situ Raman spectroscopy of amorphous calcium phosphate to crystalline hydroxyapatite transformation, *MethodsX*, 2018, **5**, 1241–1250, DOI: **10.1016/j.mex.2018.09.015**.

87 A. Ghita, F. C. Pascut, V. Sottile and I. Notingher, Monitoring the mineralisation of bone nodules in vitro by space- and time-resolved Raman micro-spectroscopy, *Analyst*, 2014, **139**(1), 55–58, DOI: **10.1039/c3an01716h**.

88 E. M. Czekanska, M. J. Stoddart, J. R. Ralphs, R. G. Richards and J. S. Hayes, A phenotypic comparison of osteoblast cell lines versus human primary osteoblasts for biomaterials testing, *J. Biomed. Mater. Res., Part A*, 2014, **102**(8), 2636–2643, DOI: **10.1002/jbm.a.34937**.